Seasonal and interannual variations of the North Equatorial Current bifurcation in a high-resolution OGCM

Yoo Yin Kim,[1] Tangdong Qu,[1] Tommy Jensen,[1] Toru Miyama,[2] Humio Mitsudera,[3] Hyoun-Woo Kang,[5] and Akio Ishida[4]

Received 19 June 2003; revised 13 January 2004; accepted 30 January 2004; published 24 March 2004.

[1] The variation of the North Equatorial Current (NEC) bifurcation is investigated using results from a high-resolution ocean general circulation model (OGCM). The bifurcation occurs at about 15.5°N for the annual average and is easily identifiable in the upper 500 m, but it varies with time and depth. In agreement with recent observations, during the summer season the NEC bifurcation moves equatorward with a weak poleward shift with depth, while a large poleward movement with a poleward shift with depth is found during the winter season. Vertical mode decomposition indicates that the seasonal variation of the NEC bifurcation is dominated by the first two baroclinic modes. On the interannual timescale, the meridional migration of the NEC bifurcation is strongly influenced by El Niño/Southern Oscillation (ENSO); its correlation with the Southern Oscillation Index exceeds 0.8 in magnitude at depths around the thermocline. The NEC bifurcation occurs at its northernmost position during El Niño years and at its southernmost position during La Niña years. This variation is mainly accounted for by westward propagation of upwelling (downwelling) Rossby waves generated by winds in the central equatorial Pacific and by an anomalous anticyclone (cyclone) located in the western North Pacific when a warm (cold) event matures. The interannual variability of the NEC transport is highly correlated with that of the Mindanao Current (MC) and the Kuroshio transports. It is also found that the interannual variability of the NEC bifurcation latitude is highly correlated with the variations of transports in the NEC and the Kuroshio, but is less correlated with transport variations in the MC. *INDEX TERMS:* 4576 Oceanography: Physical: Western boundary currents; 4572 Oceanography: Physical: Upper ocean processes; 4512 Oceanography: Physical: Currents; 4231 Oceanography: General: Equatorial oceanography; 4215 Oceanography: General: Climate and interannual variability (3309); *KEYWORDS:* bifurcation, seasonal, interannual

Citation: Kim, Y. Y., T. Qu, T. Jensen, T. Miyama, H. Mitsudera, H.-W. Kang, and A. Ishida (2004), Seasonal and interannual variations of the North Equatorial Current bifurcation in a high-resolution OGCM, *J. Geophys. Res.*, *109*, C03040, doi:10.1029/2003JC002013.

1. Introduction

[2] The North Equatorial Current (NEC) bifurcates into the northward flowing Kuroshio and the southward flowing Mindanao Current (MC) after it meets the western boundary at the Philippine coast [*Schott*, 1939; *Toole et al.*, 1990]. An important indicator of the partition of the NEC mass, heat, and salt transport between the Kuroshio and the MC is the bifurcation latitude of the NEC. Because of this bifurcation, part of the North Pacific Water is able to penetrate into the tropical circulation through the MC [*Fine et al.*, 1994]. The NEC, the MC, and the Kuroshio in the western North Pacific exhibit strong seasonal and interannual variabilities since they are in a geographical location where dynamic processes are dominated by the monsoons and El Niño-Southern Oscillation (ENSO). It is therefore reasonable to expect that the NEC bifurcation latitude also varies seasonally and interannually.

[3] According to Sverdrup theory, the NEC should bifurcate at the zero line of zonally integrated wind stress curl. This simple steady theory is, however, not sufficient to understand the actual bifurcation latitude of the NEC. It masks the variable interactions and exchanges of the water masses between oceanic gyres. In reality, surface wind varies both in time and space, and these variations make a significant impact on the NEC bifurcation latitude by both the local Asian monsoon and remote Rossby waves [*Qiu and Lukas*, 1996]. Another limitation of the Sverdrup theory is that it does not explain the depth dependence of the NEC bifurcation latitude, which shifts from about 13°N near the surface to as far north as 20°N at depths around 800 m [*Qu et al.*, 1998, 1999; *Qu and Lukas*, 2003]. This northward

[1] International Pacific Research Center, SOEST, University of Hawaii at Manoa, Honolulu, Hawaii, USA.
[2] Frontier Research System for Global Change, Yokohama, Japan.
[3] Institute of Low Temperature Science, Hokkaido University, Sapporo, Japan.
[4] Ocean Observation and Research Department, Japan Marine Science and Technology Center, Yokosuka, Japan.
[5] Korea Ocean Research and Development Institute, Ansan, Korea.

0148-0227/04/2003JC002013$09.00

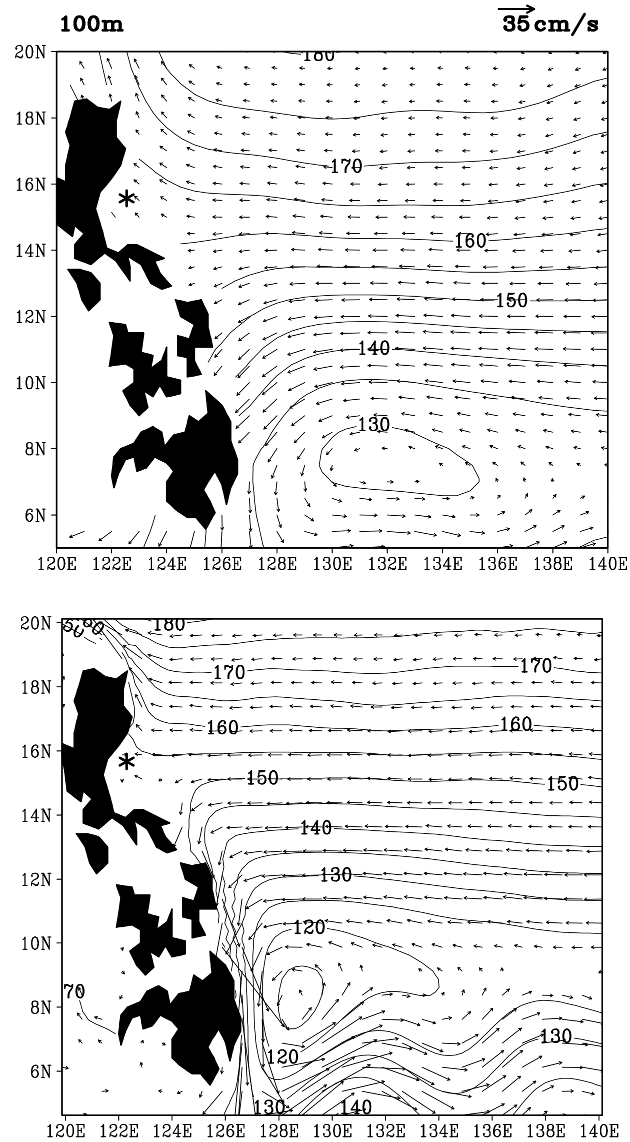

Figure 1. Annual mean dynamic height (dyn cm) and geostrophic flow. (top) Observation at 100 m relative to 1200 m from *Qu and Lukas*' [2003]) historical hydrographical data. (bottom) Model at 100 m relative to 1007 m from OGCM. The asterisks indicate the depth-averaged NEC bifurcation points.

shift of the NEC bifurcation latitude with depth was interpreted as a result of the poleward contraction of the subtropical gyre on denser waters [*Reid and Arthur*, 1975].

[4] Since the flow field in the low-latitude western Pacific is highly variable and complex, a general description of the NEC bifurcation latitude variations has been difficult to obtain due to lack of observations. Recently, *Qu and Lukas* [2003] prepared a new climatology by using historical temperature and salinity data. Increased resolution of the new climatology allowed them to provide the first observational evidence on the depth dependence and seasonal variation of the NEC bifurcation latitude. They showed that the bifurcation of the NEC occurs at the southernmost position in July and the northernmost position in December and that it shifts northward with increasing depth. Their analysis did not include interannual variability of the bifurcation due to data limitation.

[5] The interannual variation of the NEC bifurcation has been examined by *Qiu and Lukas* [1996] using a reduced-gravity model. They showed that the positive wind stress curl of the trade wind tends to intensify and shifts the NEC bifurcation latitude northward in the year before El Niño events and these changes influence the midlatitude, subtropical circulation via the Kuroshio. However, due to the limited vertical structure and the absence of Indonesian Throughflow of the model, the representation of their results needs to be further examined, and in particular, the variation of the NEC bifurcation latitude at intermediate depths remains unknown. In this study, we use results from a high-resolution ocean general circulation model (OGCM) to estimate the seasonal and interannual variations of the bifurcation latitude and to identify the oceanic processes controlling these variations.

[6] The paper is arranged as follows. Section 2 briefly describes the model and its validation with observations. Section 3 presents the seasonal variation of the NEC bifurcation latitude and its depth dependence. Section 4 focuses on interannual variation of the NEC bifurcation latitude and its relationship to the ENSO. The interannual variations of transport in the NEC, the MC, and the Kuroshio are also examined in this section. Results are summarized and discussed in section 5.

2. Model Description and Validation

2.1. Model Description

[7] The model used for this study is the Japan Marine Science and Technology Center (JAMSTEC) OGCM [*Ishida et al.*, 1998], based on Modular Ocean Model version 2 [*Pacanowski*, 1995]. It covers a global domain except for the Arctic Ocean extending from 75°S to 75°N, and has realistic coastline and bottom topography based on the National Geophysical Data Center data set (ETOPO5). The model has a horizontal resolution of 0.25° both in longitude and latitude and has 55 levels in the vertical. The vertical grid spacing increases smoothly from 10 m at the surface to about 50 m near 500 m, about 70 m near 1000 m depth, and about 400 m at 6000 m. Data of the upper 32 levels (0–1007.29 m) are used for this study.

[8] The model was spun up from an initial condition given by the annual averaged temperature and salinity of *Levitus* [1982] climatology. It was forced with the annual mean wind stress of *Hellerman and Rosenstein* [1983] during the first two model years and with the Hellerman-Rosenstein monthly mean wind stress for 18 years. For horizontal turbulent mixing, a highly scale-selective biharmonic operator was used, with a coefficient of -1×10^{19} $cm^4 sec^{-1}$ for both momentum and tracers. The vertical mixing follows the Pacanowski and Philander (1981) formulation, and no isopycnal thickness mixing parameterization is incorporated. Then, the model was further integrated for 17 years from 1982 to 1998 with 3-day averaged ECMWF wind stresses and surface relaxation to Reynolds sea surface temperature (SST) and to climatological sea surface salinity (SSS). The simulation data

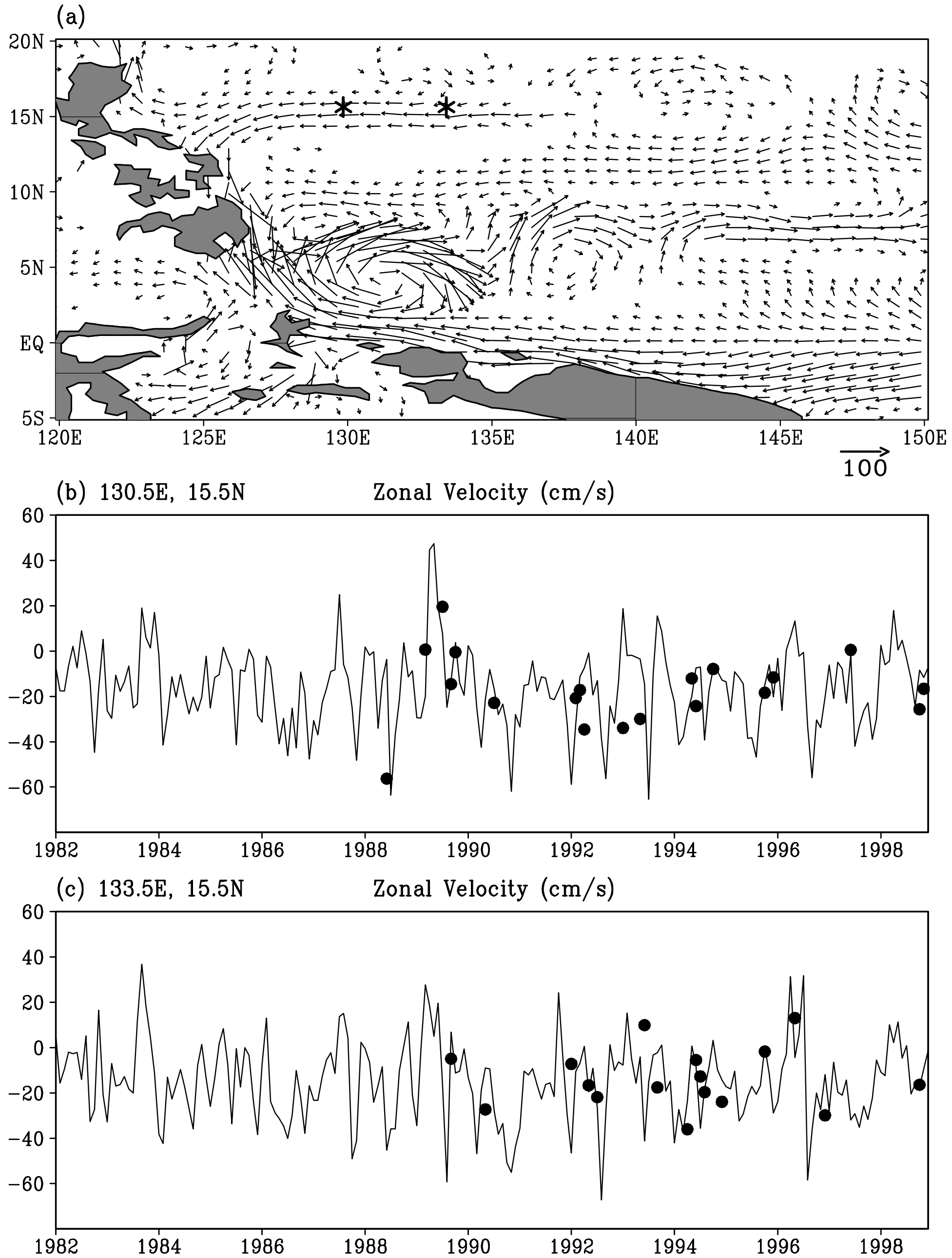

Figure 2. (a) Model mean current vector field at a depth of 15 m for July–September 1988 to compare with drifter velocity vectors averaged by 1° squares, July–September 1988 of *Lukas et al.* [1991]. Zonal currents at a depth of 15 m at (b) 130.5°E, 15.5°N and (c) 133.5°E, 15.5°N for the OGCM (solid line) and drifter zonal velocities (solid circle) from AOML.

were stored every 5 days, and they were averaged into monthly data for the present analysis.

2.2. Model Validation

[9] The JAMSTEC model reproduces reasonably well the circulation and thermal structure of the western Pacific, including the sharp thermocline in the equatorial region, the separation of the Kuroshio from the Japanese coast, and many detailed phenomena associated with the narrow western boundary currents [*Ishida et al.*, 1998]. Standard deviation of the sea surface height from the JAMSTEC model agreed with that from TOPEX/Poseidon data as well as the Parallel Ocean Program (POP) model [*Fu and Smith*, 1996]. The Kuroshio Extension was simulated better by the JAMSTEC model than by the POP model [*Ishida et al.*, 1998]. Annual mean zonal velocities from the JAMSTEC model, the POP model, and the Ocean Circulation and Climate Advanced Modeling (OCCAM) model were also compared by *Donohue et al.* [2002]. The JAMSTEC model produced the strongest and most realistic subsurface countercurrents because of the model's superior vertical resolution.

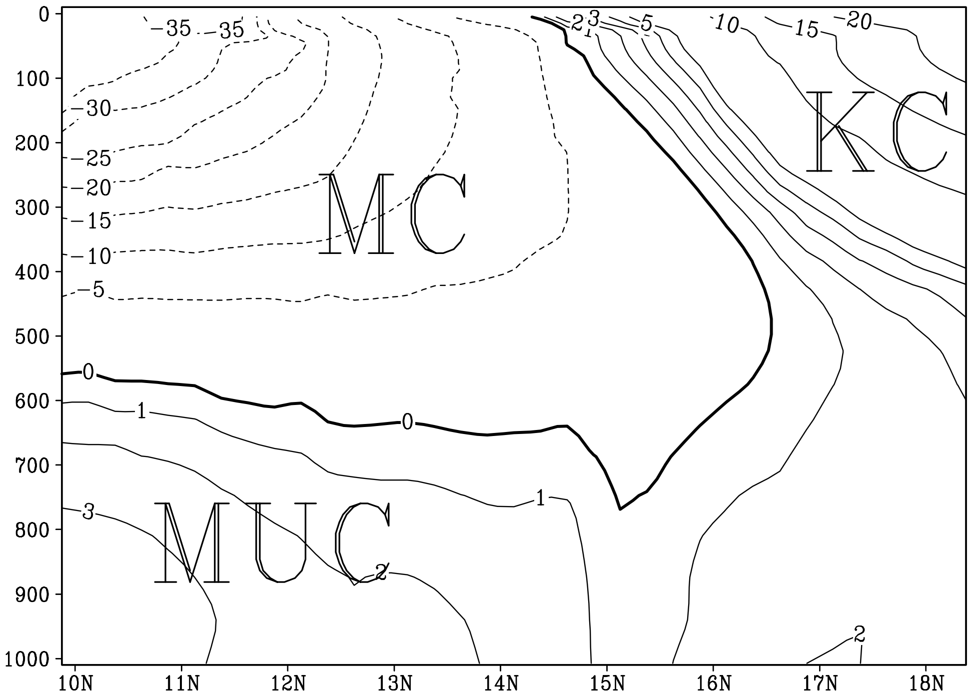

Figure 3. Annual mean meridional velocity (cm/s) averaged within a 2° longitude band off the Philippine coast. Positive value indicates northward flow, and the contour of zero velocity represents the NEC bifurcation with the Mindanao Current (MC) and Kuroshio (KC). The MUC represents the Mindanao Undercurrent.

[10] Figure 1 shows the annual mean geostrophic flow inferred from dynamic height from the *Qu and Lukas* [2003] climatology and the model. Here geostrophic calculation of the model results was based on a 1000-m reference level, 200 m shallower than that used by *Qu and Lukas* [2003], simply because only the upper 1007 m of model data were available to us. In general, these velocity estimates are consistent except in the region south of about 10°N, where *Qu and Lukas*'s [2003] climatology does not capture the wavelike structures in the North Equatorial Counter Current (NECC), presumably a result of smoothing. We define the division between the tropical and subtropical gyres at the western boundary (i.e., the NEC bifurcation) as the depth-averaged bifurcation latitude in the upper 522 m. It occurs around 15.5°N and 15.4°N in the model and the observation, respectively.

[11] For synoptic model-data comparison, we also created a mean absolute velocity field at 15 m for July–September 1988 (Figure 2a), which looks similar to the mean flow field derived from drifter data for the same period presented by *Lukas et al.* [1991, Figure 3]. The Mindanao and Halmahera eddies, the NEC bifurcation at the western boundary, and the wavelike structures of the NECC are all reproduced by the model. For the interannual variation, we compared model results with drifter data maintained by the Drifter Data Center at the Atlantic Oceanographic and Meteorological Laboratory (AOML) of National Ocean and Atmospheric Administration (NOAA). Around the NEC bifurcation latitude at 15.5°N, 130.5°E and 15.5°N, 133.5°E (asterisks in Figure 2a), where the flow is dominantly westward, the model and the drifter data show a remarkable agreement (Figures 2b and 2c). Therefore we are confident that the simulated flow fields are representative for the region studied.

3. Seasonal Variations

[12] Monthly model absolute velocity, temperature, and salinity fields from January 1982 to December 1998 were averaged to estimate the mean annual cycle, and this climatology was then used to investigate the mean seasonal cycle of the NEC bifurcation latitude.

3.1. NEC Bifurcation Latitude

[13] With the model climatology created above, we define the NEC bifurcation as a point where 2° longitude averaged meridional velocity from the Philippine coast is zero. The NEC bifurcation at the Luzon Strait (18.5°N–22°N) is not considered here. *Qu and Lukas* [2003] used a 5° longitude band because the western boundary currents derived from historical data were considerably weaker and wider. In the model, the width of the longitudinal averaging has little effect on the estimated bifurcation latitude except for the surface layer where Ekman drift occurs. For the annual average the bifurcation occurs at about 14.3°N near the surface, and it shifts to the north with increasing depth, extending north of 16.6°N at 500 m (Figure 3). Below the MC, the northward flow associated with the Mindanao Undercurrent [*Hu et al.*, 1991; *Lukas et al.*, 1991; *Qu and Lukas*, 2003] is evident.

[14] Figure 4 shows the bifurcation of the NEC for each month in the upper 522 m, where the annual mean bifurcation is well defined (Figure 3). The latitude of zero

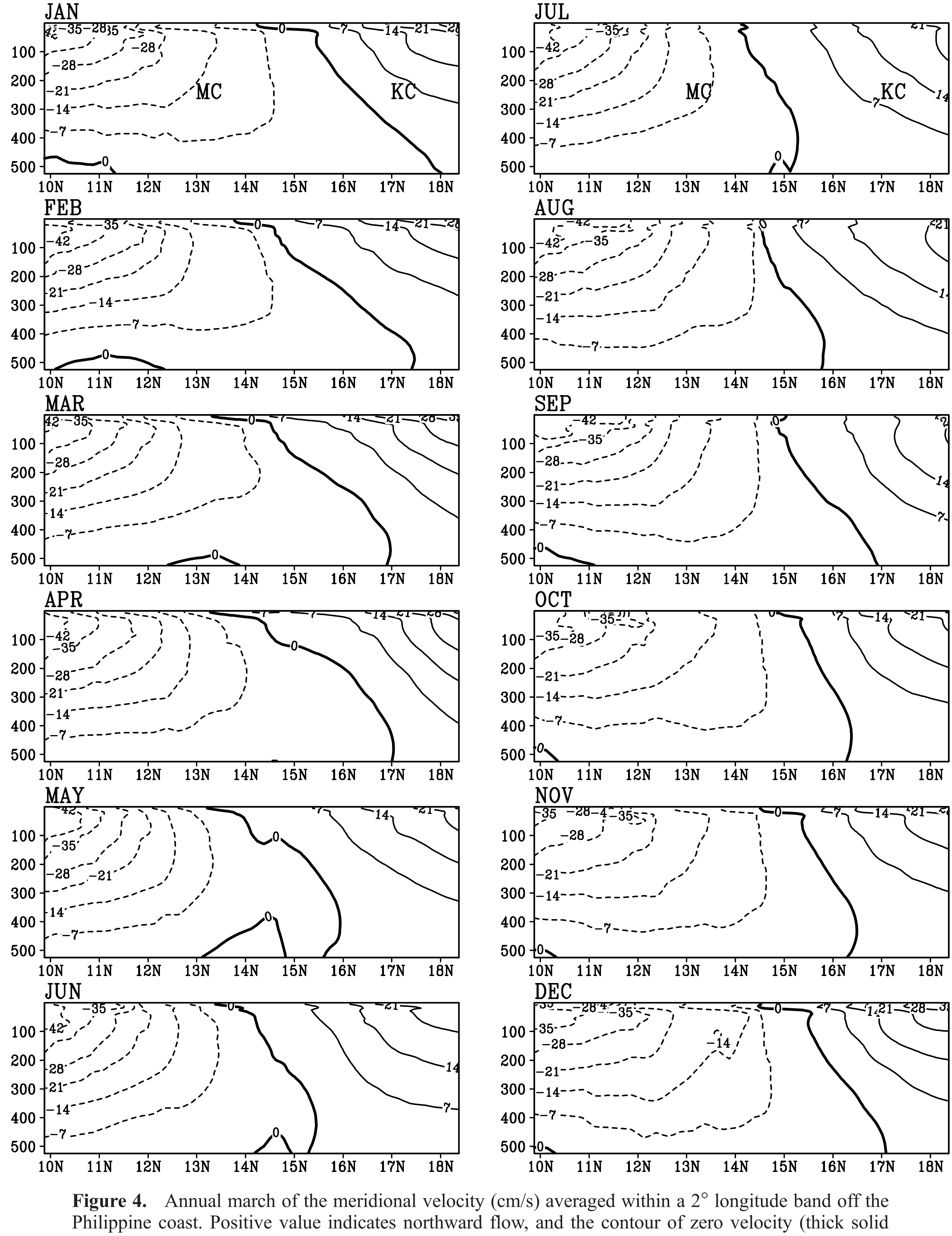

Figure 4. Annual march of the meridional velocity (cm/s) averaged within a 2° longitude band off the Philippine coast. Positive value indicates northward flow, and the contour of zero velocity (thick solid line) represents the NEC bifurcation.

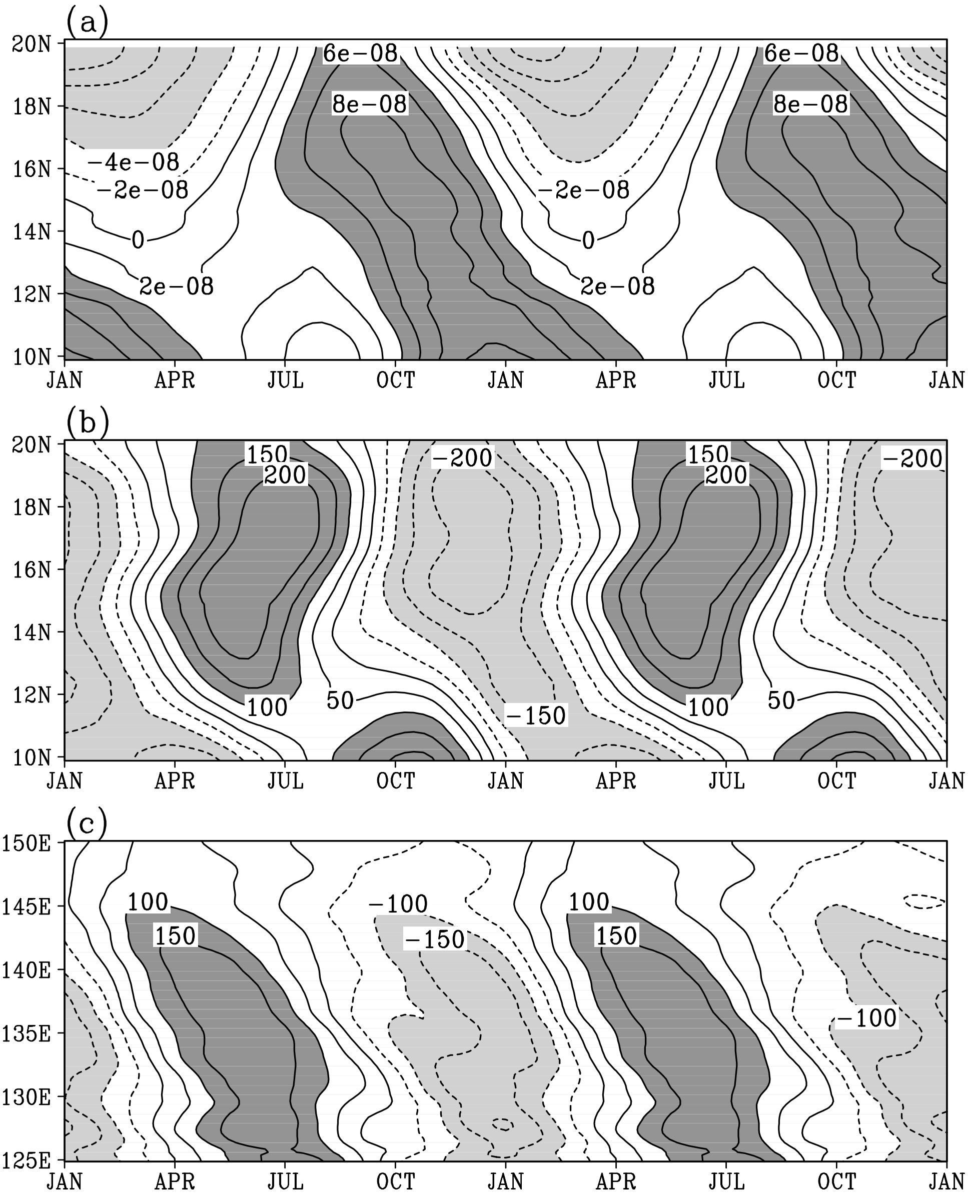

Figure 5. (a) Time-latitude plot of the ECMWF wind stress curl (N/m^3) averaged from 123°E to 135°E. (b) Time-latitude plot of the model layer heat storage (°C m) averaged from 123°E to 135°E. (c) Time-longitude plot of the model layer heat storage (°C m) averaged from 10°N to 20°N.

meridional velocity at each level moves toward its northernmost position with a large shift with depth during winter and toward its southernmost position with a weak shift with depth during summer. Near the surface, the southernmost bifurcation (13.2°N) is found in May and the northernmost bifurcation (15.1°N) in September. At deeper levels, this bifurcation shifts northward, approaching 15.1°N in July and 18.0°N in January at depths around 500 m. These seasonal variations of the bifurcation are consistent with the observations [*Qu and Lukas*, 2003], except near the surface. Ekman current driven by local Asian monsoon causes an equatorward shift of the bifurcation latitude during some months in the model. The maximum shift, more than 1° in latitude, is in January, with relatively large shifts of the bifurcation from October to June. Much smaller impact of Ekman current is found from July to September (Figure 4). Another important feature is the shallower vertical confinement of the NEC bifurcation in early summer, when the weak Mindanao Undercurrent tends to be connected with the deep extension of the Kuroshio [*Qu and Lukas*, 2003].

3.2. Upper Layer Heat Storage

[15] The NEC bifurcation is mainly confined between the sea surface and the 26.7 σ_θ surface, and layer heat storage (LHS) within these depths is a good proxy for the depth of thermocline in the western Pacific [*Qu et al.*, 1998]. Thus the changes in the LHS are directly related to the meridional movement of the NEC bifurcation. In this section we investigate the seasonal variation of the LHS.

[16] The seasonal variation of the LHS in the upper layer is mainly due to the local Ekman pumping (Figures 5a

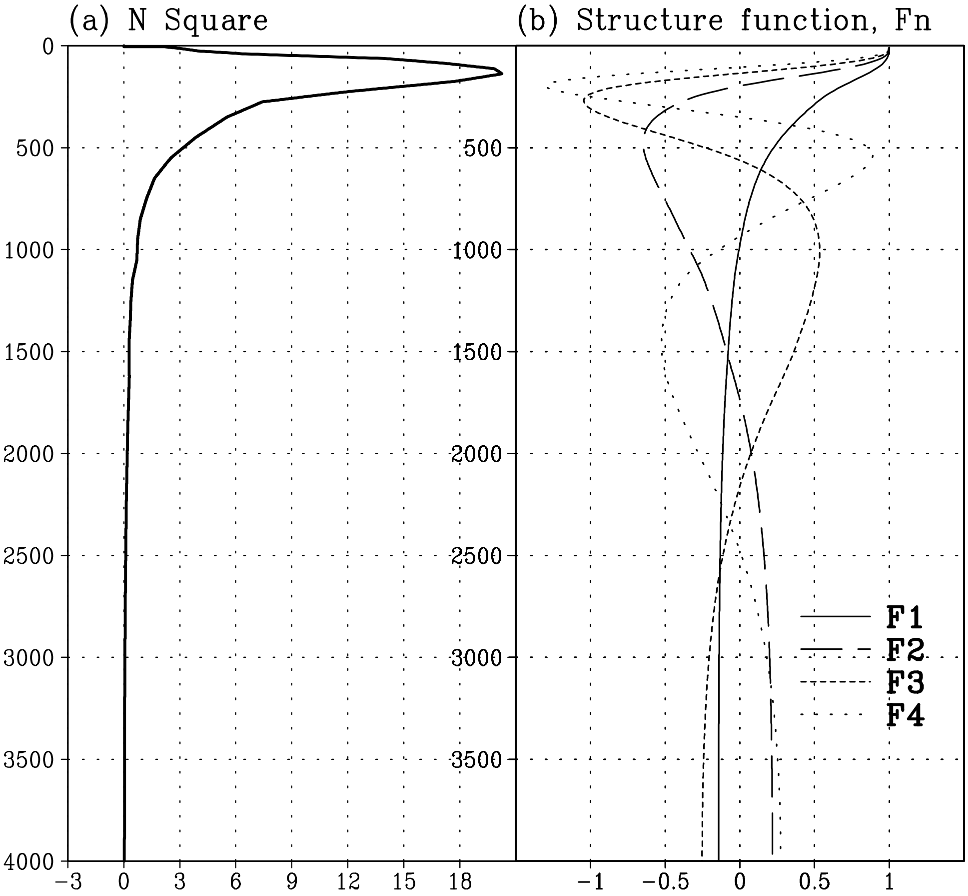

Figure 6. (a) Annual mean Brunt - Väisälä frequency N^2 (z) averaged between 120°E and 140°E at 15°N. (b) Set of orthogonal modes, F_n (z), obtained from N^2 (z) of Figure 6a.

and 5b) and the westward propagation of remotely forced Rossby waves (Figure 5c). The local Ekman pumping contains a strong annual signal associated with the Asian monsoon and the meridional movement of the Intertropical Convergence Zone (ITCZ) (Figure 5a). The zonally averaged, positive wind stress curl and the associated downward pumping have a larger meridional extent than the negative wind stress curl. The latter is mainly confined to the north of 15°N. Low LHS is a response to strong positive wind stress curl, and this indicates an anomalous cyclonic circulation in winter, whose southward component near the western boundary causes the NEC bifurcation to occur at a higher latitude (Figure 5b). During the southwest monsoon, in contrast, weaker wind stress curl produces an anomalous anticyclonic circulation whose northward component near the western boundary results in a shift of the NEC bifurcation to its southernmost position [*Qu and Lukas*, 2003]. With a lag of about 2–3 months (2 months in August to 3 months in January), the wind stress curl leads the LHS anomaly field (Figures 5a and 5b). The upward (downward) Ekman pumping integrated over time results in a rising (deepening) thermocline. Consistently, the phase relation is such that the Ekman pumping leads the thermocline displacement.

[17] The propagation of the LHS anomalies in winter is different from those in summer. The anomalies show generally a southward propagation south of 13°N–15°N (Figure 5b), presumably due to the ITCZ movement (Figure 5a). In the north, between 15°N and 19°N, there is a weak northward propagating signal in summer (Figure 5b), and this signal is related to the negative wind stress curl which leads the LHS anomalies by 2–3 months (Figure 5a). As a result, the negative (positive) LHS anomalies caused by the positive (negative) wind stress curl make the tropical gyre extend to the north (south) and the bifurcation latitude move northward (southward).

[18] To examine the influence of the westward propagation of Rossby waves, in Figure 5c we include the LHS anomaly averaged from 10°N to 20°N. Here the westward propagation from around 145°E is evident, indicating that the westward propagation of Rossby waves also plays an important role in determining the LHS variation and thus the NEC bifurcation latitude. Because of these Rossby waves, the warm and cold anomalies generated west of 145°E are conveyed into the Philippine coast, and the corresponding deepening and shoaling of the thermocline result in a southward movement of the NEC bifurcation in summer and a northward movement in winter, respectively. These results confirm that both local and remote forcing can play a role in the seasonal variation of the NEC bifurcation as suggested by earlier works [*Qiu and Lukas*, 1996; *Qu and Lukas*, 2003].

3.3. Vertical Modes

[19] In this section, we examine the most important baroclinic modes involved in the bifurcation. We find that

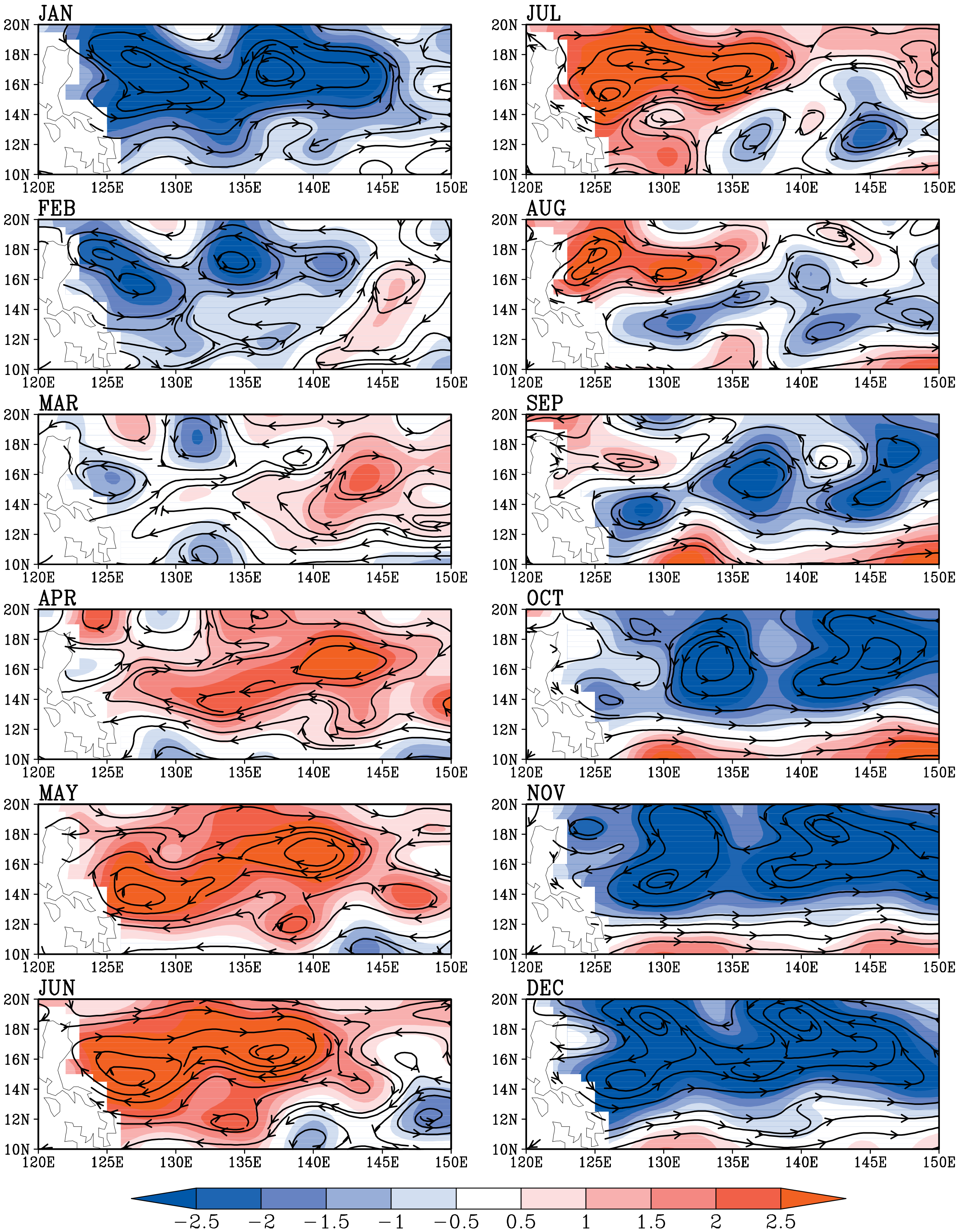

Figure 7a. Annual march of the first vertical mode of the model flow streamlines and dynamic height anomalies (dyn cm).

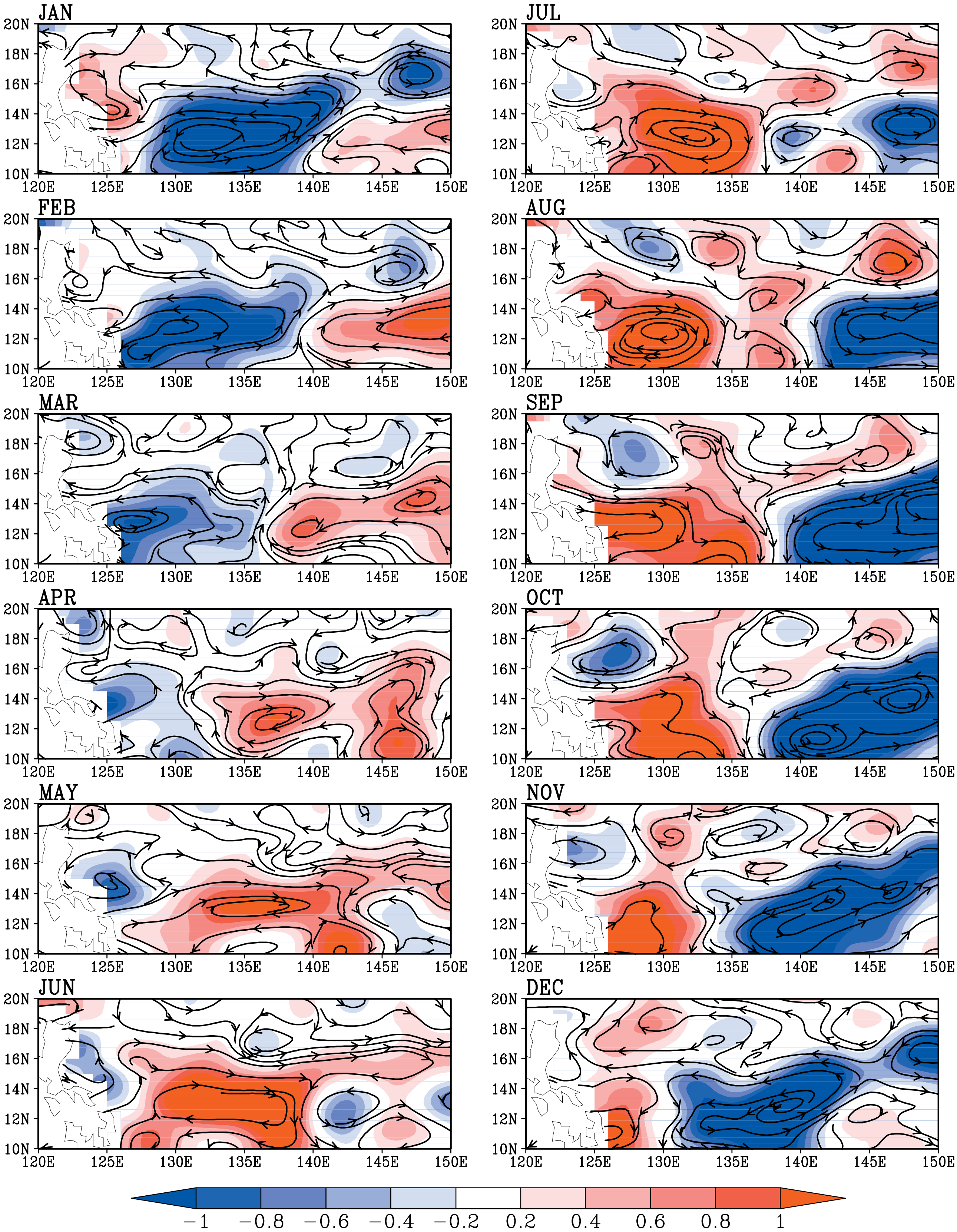

Figure 7b. Annual march of the second mode of the model flow streamlines and dynamic height anomalies (dyn cm).

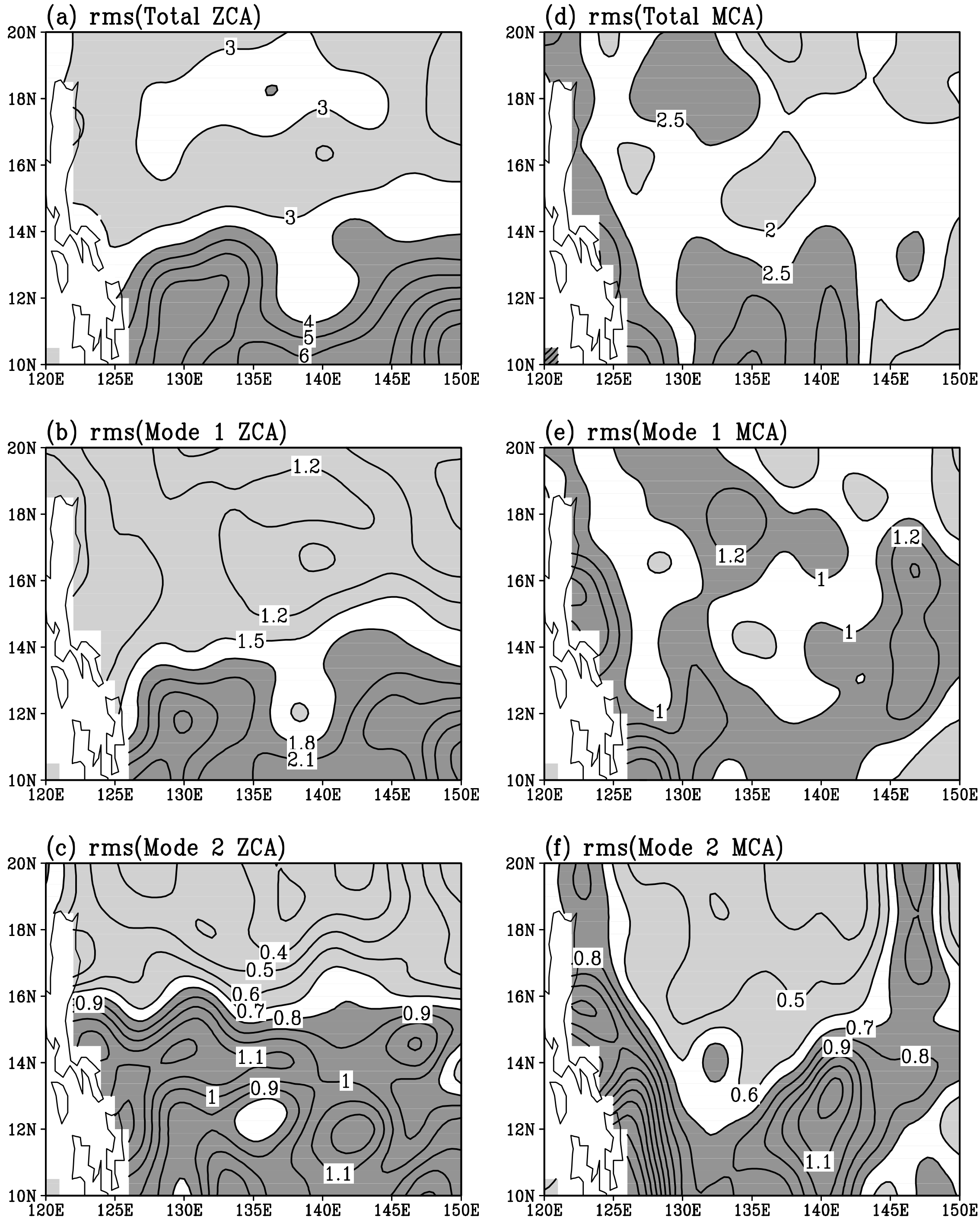

Figure 8. Maps of RMS of (a) the surface zonal current anomalies (ZCA) estimated from the average of the model top 500 m, (b) the first vertical mode of the ZCAs, (c) the second vertical mode of the ZCAs, (d) the surface meridional current anomalies (MCAs) estimated from the average of the model top five levels, (e) the first vertical mode of the MCAs, and (f) the second vertical mode of the MCAs, Units are cm/s.

only the two gravest modes are contributing significantly. The Brunt-Väisälä frequency is determined from the annual-mean density field calculated from the temperature and salinity of *Levitus* [1982] between 120°E and 140°E at 15°N, and it is interpolated vertically to a 10-m resolution up to 4000 m using a linear interpolation (Figure 6a). We compute the normal modes based on this vertical profile of N using standard techniques [*Gill*, 1982]. The structure functions are shown in Figure 6b, and they are applied to projections of the model flow and the model dynamic height interpolated vertically to the same resolution as N. The vertical profiles of the simulated current anomalies are

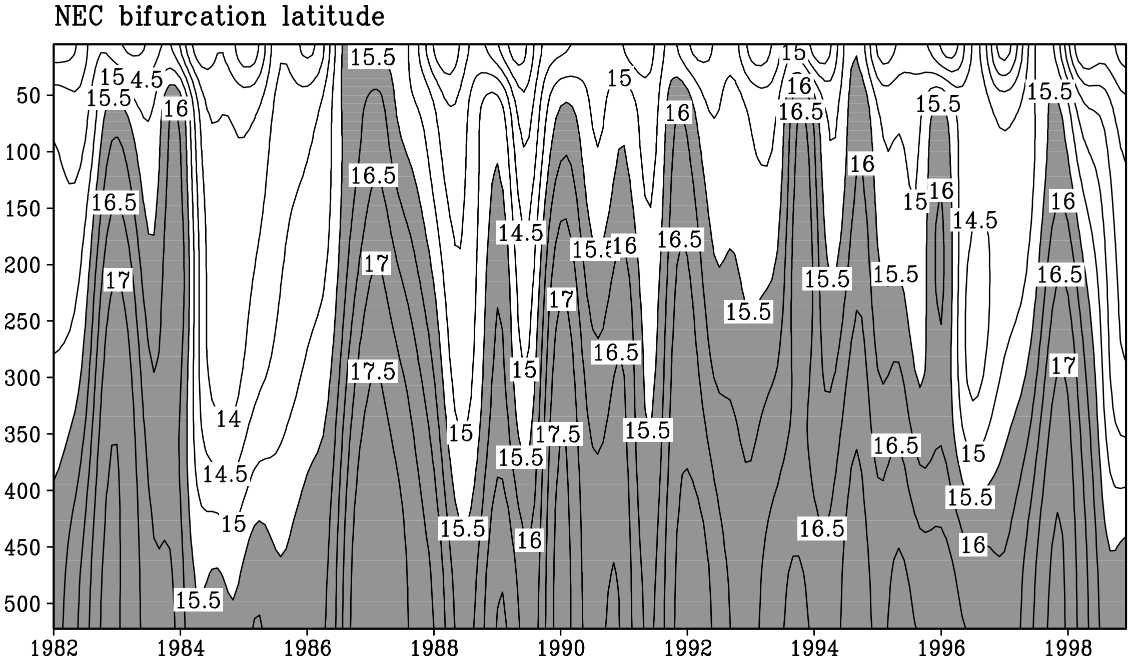

Figure 9. Time-depth section of the NEC bifurcation latitude in upper depths above 522 m.

projected onto each orthogonal vertical mode using model data to the bottom.

[20] Figures 7a and 7b show streamlines calculated from zonal and meridional current anomalies (ZCAs and MCAs) and dynamic height anomalies (DHAs) for the first and the second baroclinic vertical mode, respectively. The northward shift of the bifurcation latitude with depth is due to the vertical structure function of the first and the second modes that change sign at about 800 m and 200 m, respectively (Figure 6). For mode 1, larger values of the anomalies extend meridionally to the north of 15°N, whereas variability of mode 2 is more confined to the south of that latitude. Although the magnitudes of the anomalous circulation in the second mode are smaller than those in the first mode, westward DHA propagation appears to be equally dependent on both modes.

[21] The streamlines and DHAs of the first mode explicitly show that anomalous cyclonic (anticyclonic) circulation caused by the Asian winter (summer) monsoon is closely related to the meridional excursion of the NEC bifurcation latitude (Figure 7a). When the northeast monsoon prevails in winter, strong Ekman pumping due to positive wind stress curl produces an anomalous cyclonic circulation (negative DHA). On the other hand, as the southwest monsoon develops, local Ekman pumping reaches its seasonal minimum [*Qu and Lukas*, 2003] and thus produces an anomalous anticyclonic circulation (positive DHA). Westward propagation of remotely generated Rossby waves is also evident in the first mode. Therefore both the local Ekman pumping and propagating Rossby waves play an important role in the formation of the anomalous circulation and thus in the meridional movement of the NEC bifurcation latitude.

[22] For the second mode, we find that current anomalies generated in the central Pacific propagate northward when they reach the southern part of the Philippine coast. This northward propagation of the anomalous circulation influences the NEC bifurcation. For instance, a negative DHA with an anomalous cyclonic circulation gyre at 150°E propagates westward and become gradually stronger from July to January, and it rapidly weakens when it encounters the southern part of the western boundary. Then the anomalous cyclonic gyre moves northward from February to June, which prevents the NEC bifurcation from moving as far south as expected from the intense anomalous anticyclonic gyre of the first mode. Another anomalous cyclonic circulation gyre is located at the northern part of the Philippine Sea from October to March, which enhances the northward movement of the bifurcation through the larger anomalous cyclonic circulation gyres of the first vertical mode (Figures 7a and 7b). The opposite (same) circulation gyres in both modes in summer (winter) will reduce (increase) the seasonal vertical slope of the bifurcation latitude as shown in Figure 4, which implies that the seasonal vertical slope change can be accounted for by the mutual interplay between the first and the second baroclinic vertical modes.

[23] Figure 8 illustrates the contribution of the first two modes to the variation of the surface currents. Because the vertical functions for these two modes have no vertical shear in the top 50 m, the surface current anomaly here is calculated by averaging over the five uppermost levels of the model (depth 10 m to 50 m). The root mean squares (RMS) of the surface zonal current anomalies (ZCAs) and meridional current anomalies (MCAs) are large over the Mindanao dome and along the Philippine coast (Figures 8a and 8d). Their spatial distribution shows a good agreement with that explained by the first vertical mode, suggesting that the first mode is by far the most important contribution to the surface current variability (Figures 8b and 8e). The

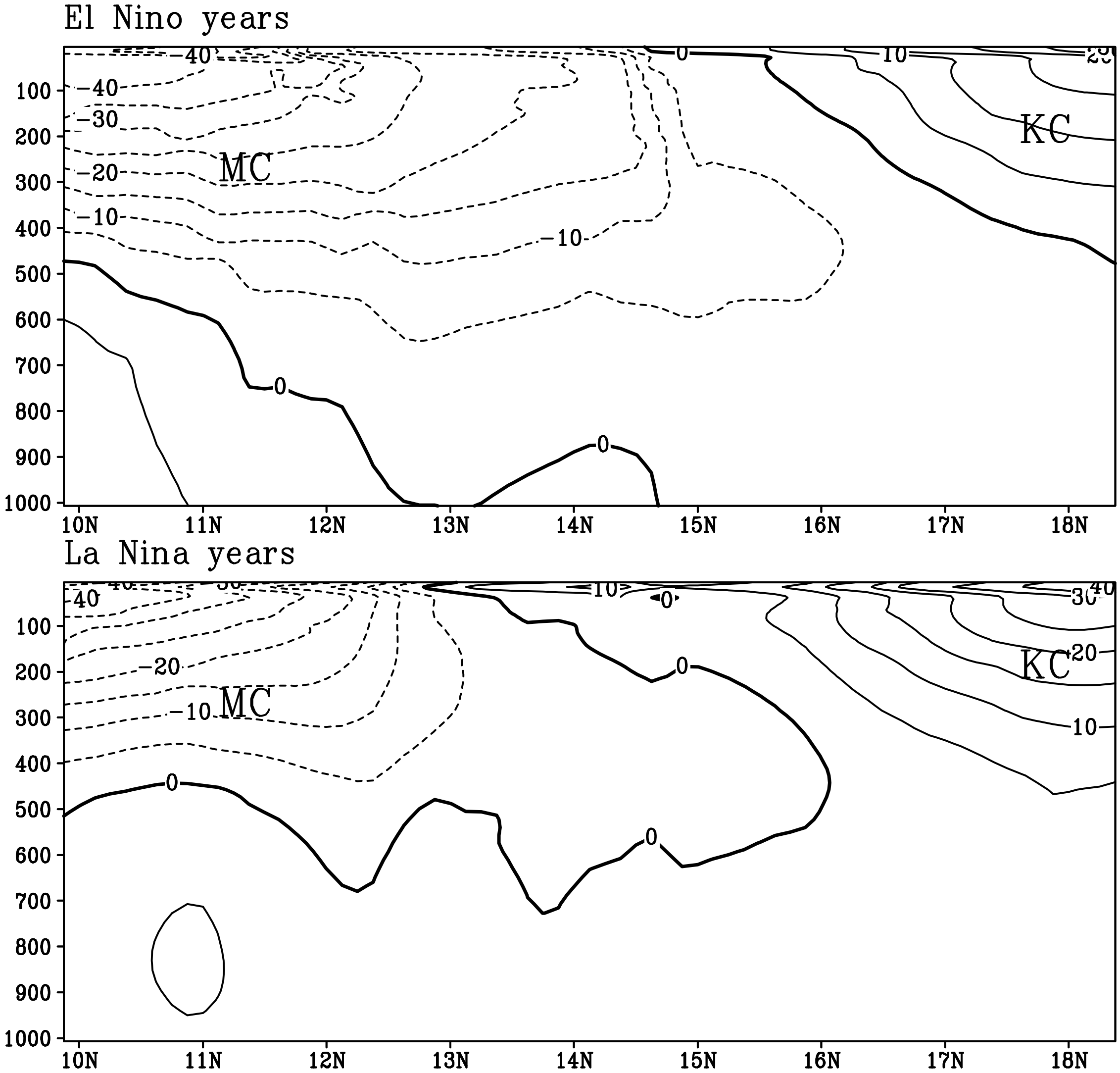

Figure 10. (top) El Niño composite of the meridional velocity (cm/s) averaged within a 2° longitude band off the Philippine coast. (bottom) La Niña composite of the meridional velocity (cm/s) averaged within a 2° longitude band off the Philippine coast. Positive value indicates northward flow, and the contour of zero velocity represents the NEC bifurcation.

largest variations associated with mode 2 occur near the Philippine coast (Figures 8c and 8f) and are expected to directly affect the meridional movement of the NEC bifurcation through variability of the western boundary current.

4. Interannual Variations

4.1. NEC Bifurcation Latitude

[24] Figure 9 shows the time series of the NEC bifurcation latitude in the upper 522 m. Here, a 12-month running-mean filter has been applied to remove the mean seasonal cycle. In general, the NEC bifurcation latitude has a clear relationship with ENSO. It shifts northward during El Niño years (1982/1983, 1986/1987, 1991/1992, 1997/1998) and southward during La Niña years (1984/1985, 1988/1989). Its vertical distribution is quite similar to that of the seasonal variations. To further demonstrate this correspondence, we also present the composites of the zonally averaged meridional velocities within a 2° longitude band from the Philippine coast for the winters of El Niño and La Niña years (Figure 10). The NEC bifurcation does not occur farther northward than 16°N in the upper layers and becomes unrecognizable below 600 m during winters of the La Niña years, while it extends farther northward and deeper during winters of El Niño years.

[25] Figure 11 shows the correlation between the NEC bifurcation latitude and the southern oscillation index (SOI) at each level from lagged cross correlation analysis. It reveals that the NEC bifurcation latitude varies in almost the same phase as ENSO. They are highly correlated within the main thermocline ranging from 75 m to 250 m in depth, where the correlation reaches 0.85 with SOI leading the NEC bifurcation latitude by 1 month. The cross correlation between the SOI and the NEC bifurcation latitude also has a relatively wide band and a vertically distributed pattern of the negative coefficients ($r \geq 0.6$) centered on -1-month lag and 150 m depth (Figure 11). The appearance of this wide band with ±3 months time lag, instead of a maximum at a narrowly defined time lag, may be due to the fact that

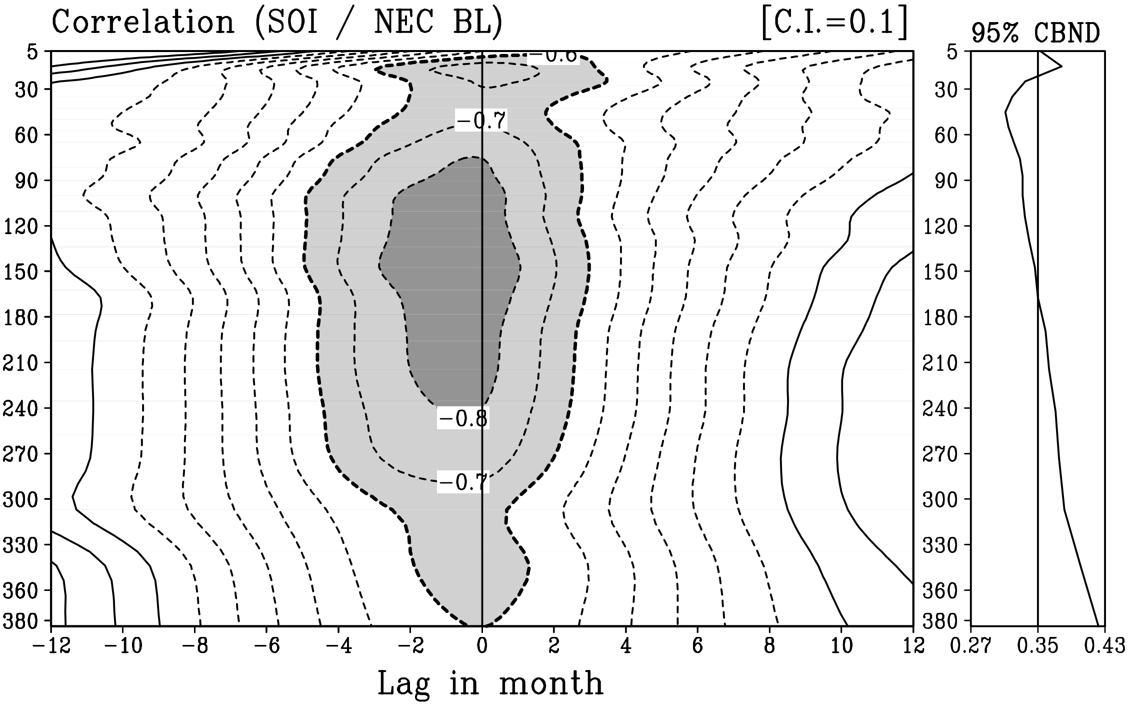

Figure 11. (left) Depth-lag (in month) section of the cross correlation between Southern Oscillation Index (SOI) and NEC bifurcation latitude. (right) Vertical profile of 95% confidence band. The region of the correlation greater than 0.6 is shaded. The contour interval (C.I.) is 0.1.

the center of wind-forcing area is located at different longitude during different ENSO events [*Qiu and Lukas*, 1996].

4.2. Zonal Wind Stress (ZWS) and Layer Heat Storage (LHS)

[26] To investigate the interannual variations in the NEC bifurcation latitude, cyclostationary empirical orthogonal function (CSEOF) analysis, with its associated multimodal regression analysis, is applied to the monthly OGCM data. The main advantage of the CSEOF method, compared to other EOF methods, is that it provides optimal monthly spatial patterns (instead of a single constant spatial pattern), whose amplitude varies interannually as a time series [*Kim and North*, 1997; *Kim and Kim*, 2002]. For example, Figure 12a shows the low-frequency amplitude variations of the monthly spatial fields. There is a different field for each month. An example (for December) is shown in Figure 12b. There are ZWS fields for each month (not shown). This technique is somewhat different from other conceptually similar tools such as extended EOFs or complex EOFs. Details of the methods, including multimodal regression analysis, are given in Appendices A and B.

[27] We apply the CSEOF analysis to Pacific surface ZWS and LHS variability. We do this to relate the meridional excursion of the NEC bifurcation latitude in the western Pacific to distinctive basin-scale ZWS and LHS variability. The year-to-year evolutions of the leading CSEOF modes, accounting for 31.8% and 26.2% of the ZWS and LHS variability, respectively, are clearly related to ENSO (Figure 13), and they are both well correlated with the normalized and band-pass filtered (2–7 years) time series of the depth-averaged NEC bifurcation latitude (Table 1). The positive peaks in the three time series appear during the mature stage of El Niño events (1982/1983, 1986/1987, 1991/1992, 1997/1998), whereas negative peaks appear during La Niña (1984/1985, 1988/1989).

[28] The ZWS spatial pattern of the leading CSEOF mode is characterized by westerly (easterly) anomalies in the central Pacific during the peak phase of El Niño (La Niña). Figure 12b shows the spatial pattern (CSLV) for December. *McPhaden et al.* [1998] also reported that the ZWS anomaly in the western and central Pacific is strongly associated with ENSO variability. Figure 12a shows the interannual evolution of the first CSEOF mode of the ZWS after removing the annual mean cycle. The spatial pattern of the first CSEOF mode shows typical ZWS patterns associated with ENSO. This pattern does not change significantly from month to month, but becomes relatively stronger in winter (Figure 12b). The ZWS anomaly in the North Pacific shows an anomalous anticyclone (cyclone) forced by westerlies (easterlies) in the northern part of the Philippine Sea and by easterlies (westerlies) in its southern part. Also, the ZWS anomaly field shows anomalous cyclonic circulation created by westerlies in the equatorial central Pacific and by easterlies in the central North Pacific. This is consistent with wind stress anomalies associated with the Pacific-East Asian teleconnection that bridges the warm (cold) events in the eastern Pacific and an anomalous anticyclone (cyclone) located in the western North Pacific [*Wang et al.*, 2000]. They demonstrated that anomalous Philippine Sea anticyclone occurs during the mature phase of warm ENSO events. In the southern part of the Philippine anticyclone (cyclone), anomalous easterlies (westerlies) prevail in the equatorial western Pacific and generate the eastern Pacific

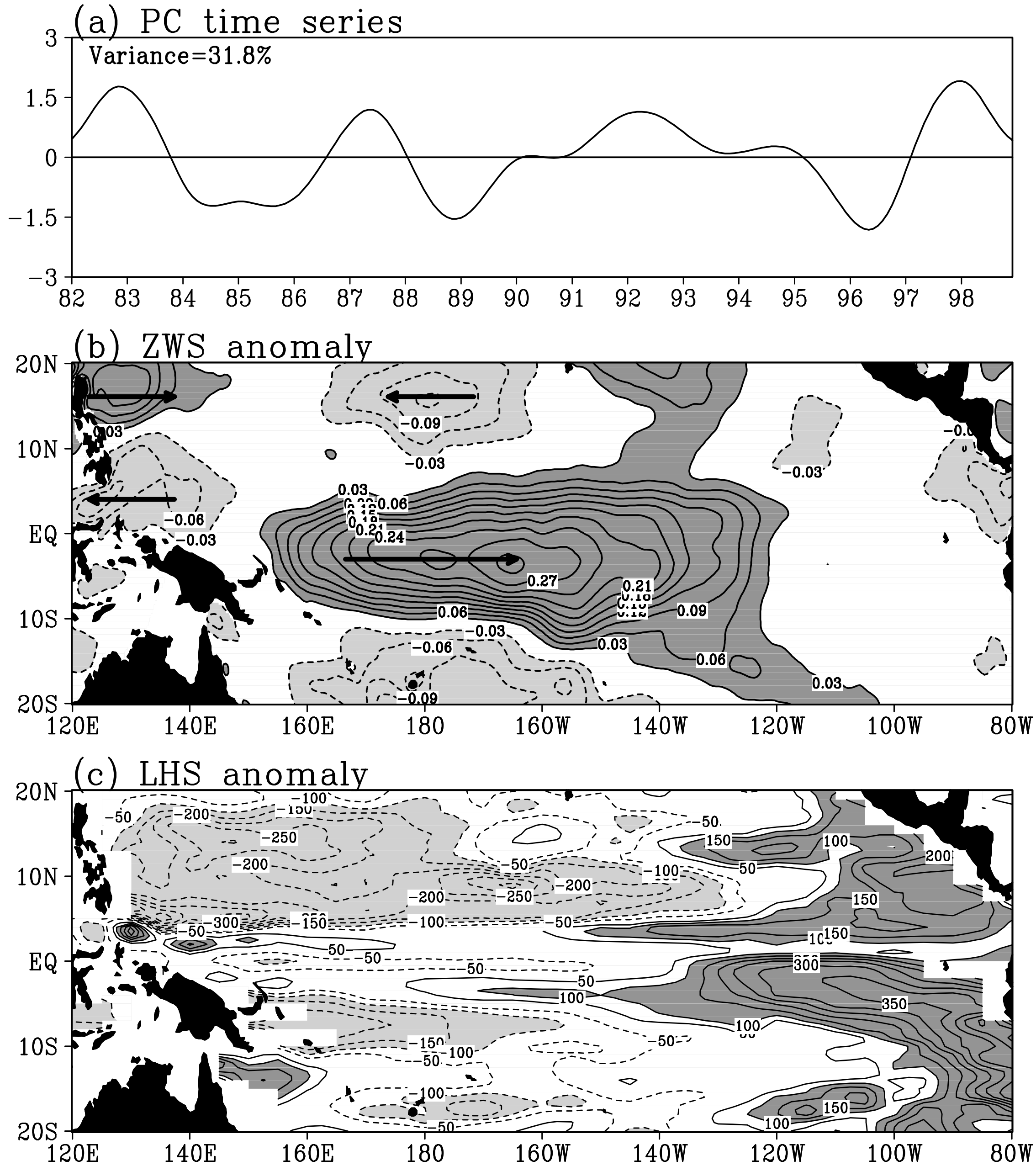

Figure 12. (a) First PC time series of the zonal wind stress (ZWS) anomaly, (b) first CSEOF mode of the ZWS anomaly in December (10^{-7} N/m^3), and (c) regressed layer heat storage (LHS) anomaly obtained from multimodal regression analysis. Its temporal evolution follows the first PC time series of the ZWS anomaly. The arrows in Figure 12b represent direction of anomalous wind circulation, which forms an anomalous cyclone or anticyclone.

warming (cooling) by the eastward propagation of oceanic equatorial upwelling (downwelling) Kelvin waves [*Boulanger and Menkes*, 1999; *Kim and Kim*, 2002].

[29] The LHS anomaly patterns (Figure 12c) are derived from multimodal regression analysis explained in Appendix B. The spatial pattern of the LHS anomaly associated with the ZWS anomaly is primarily the leading mode of the LHS anomaly field, and explains about 89.4% of the total ZWS variability (Table 2). This means that the ZWS and LHS anomalies are closely connected. Large variations of LHS in the western North Pacific are associated with basin-wide warming/cooling events related to the ENSO. Northward movement of the NEC bifurcation latitude is accompanied by a negative LHS anomaly in the western North Pacific and a positive LHS anomaly in eastern Pacific and equatorial regions. The anomalies result from the propagation of the equatorial long waves [e.g., *Wang et al.*, 1999; *Kim and Kim*, 2002]. The negative LHS anomaly in the Philippine Sea in Figure 12c is connected with the anomalous Philippine Sea anticyclone shown in Figure 12b. It is a Rossby wave response to the sea surface cooling in the western North Pacific due to the warming in the equatorial Pacific [*Wang et al.*, 2000]. The thermocline depth change in the western North Pacific tends to be in

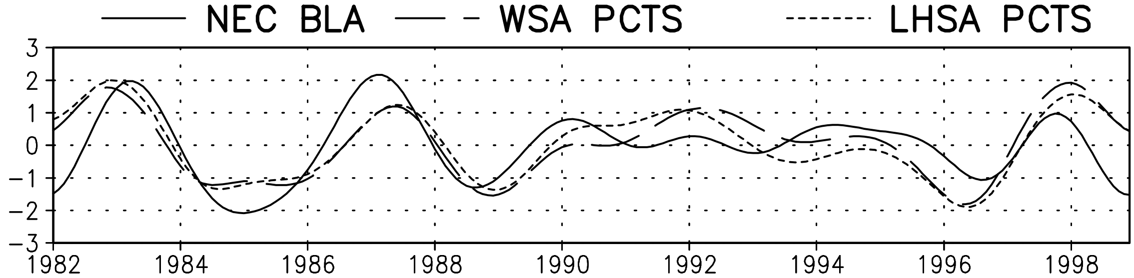

Figure 13. Band-pass filtered (2–7 years), normalized, and depth-averaged NEC bifurcation latitude (solid line), the first PC time series of the zonal wind stress anomaly (dashed line), and the first PC time series of the layer heat storage anomaly (dotted line).

phase with the equatorial eastern Pacific warming [*Wang et al.*, 1999], thereby changing the thermocline depth in the Philippine Sea through the remotely forced Rossby waves. As a result, the LHS anomaly changes occur in phase with the Philippine Sea anomalous anticyclone [*Wang et al.*, 2000]. Therefore the westerly ZWS anomalies near the date line and the anticyclone over the Philippine Sea allow a regional negative LHS anomaly. This scenario is characteristic when the NEC bifurcation latitude is located at its northernmost position. Note that the ZWS forcing tends to shift the NEC bifurcation in phase with the ENSO cycle as found from lag correlation analysis between the NEC bifurcation latitude and SOI (Figure 11).

[30] To show more details of how the spatial and the interannual variability of the ZWS and LHS anomalies are associated with the NEC bifurcation latitude variability, ZWS and LHS anomalies are reconstructed from the first CSLVs. Figures 14a and 14b show the longitude-time plot of the reconstructed ZWS anomaly along the equator and the reconstructed LHS anomaly along 15.5°N, respectively. As expected, the extreme northward (southward) shifts in the NEC bifurcation latitude (Figure 14c) correspond to westerly (easterly) ZWS anomalies in the equatorial central Pacific and negative (positive) LHS anomalies in the western North Pacific. Westward propagation of LHS anomalies associated with ENSO events can be also identified from the region between ∼125°E and ∼180° (Figure 14b). During the mature phase of El Niño (La Niña), strong negative (positive) LHS anomalies at the western North Pacific cause the NEC bifurcation to move to its northernmost (southernmost) position.

4.3. Relation Between the NEC Bifurcation and Transports

[31] The interannual variations of the NEC bifurcation latitude and the transports of the NEC, the MC, and the Kuroshio in the upper 522 m are compared in Figure 15. Large transport and northward bifurcation latitude anomalies are most prominent in the El Niño years (1982/1983, 1986/1987, and 1997/1998). As the NEC bifurcation moves northward during these events, more NEC water flows into the MC. Conversely, large Kuroshio transport and southward bifurcation latitude anomalies occur during La Niña years (1984/1985, 1988/1989, and 1996/1997). The correlations among the time series in Figure 15 are generally good, especially during the El Niño. Phase delays between them are in most cases shorter than 4 months (Table 3).

[32] The lag correlation between the model transports and the NEC bifurcation latitude gives a more quantitative comparison between their interannual fluctuations (Figure 16a). The NEC bifurcation latitude anomaly leads the transport anomalies of the NEC, the MC, and the Kuroshio by about 2 months, 1 month, and 4 months, respectively.

[33] The correlation analysis between the NEC, MC, and Kuroshio transports estimated from the high-resolution model corroborates previous observations and model studies. For instance, the high correlation between the NEC and the Kuroshio transports (Figure 16b) has previously been reported [*Yamagata et al.*, 1985; *Qiu and Joyce*, 1992; *Qiu and Lukas*, 1996; *Qu et al.*, 1998; *Gilson and Roemmich*, 2002]. Since the transport increases of the NEC near the western boundary can be linked to the ENSO, the high correlation between the NEC and the Kuroshio transports suggests that some of the ENSO signals of the NEC

Table 1. Correlation (Lag in Month) Among NEC BLA, WSA PCTS, and LHSA PCTS[a]

	NEC BLA	WSA PCTS	LHSA PCTS
NEC BLA	-	*0.64* (0)	*0.64* (−1)
WSA PCTS	*0.64* (0)	-	**0.95** (0)
LHSA PCTS	*0.64* (−1)	**0.95** (0)	-

[a]For NEC BLA, WSA PCTS, and LHSA PCTS, refer to the caption of Figure 12. The boldface and italic values indicate that the correlation is 99% and 95% significant, respectively.

Table 2. Correlation Square Value (r^2) and Percent Variance (%) Explained by Each Predictor Principle Component Time Series (PCTS) in the Multimode Regression Analysis[a]

LHSA, Mode Number	LHSA, %
1	*84.9*
2	*0.1*
3	*0.0*
4	*0.2*
5	*0.2*
6	*2.8*
7	*0.6*
8	*0.0*
9	*1.3*
10	*0.6*
$\mathbf{r^2}$	**0.953**

[a]The first 10 normalized PCTS of the layer heat storage anomaly (LHSA) field have been regressed on the first PCTS of the zonal wind stress anomaly (ZWSA) field. The number in the left column represents the LHSA mode number. The r^2 value is in boldface; percent variance is italicized.

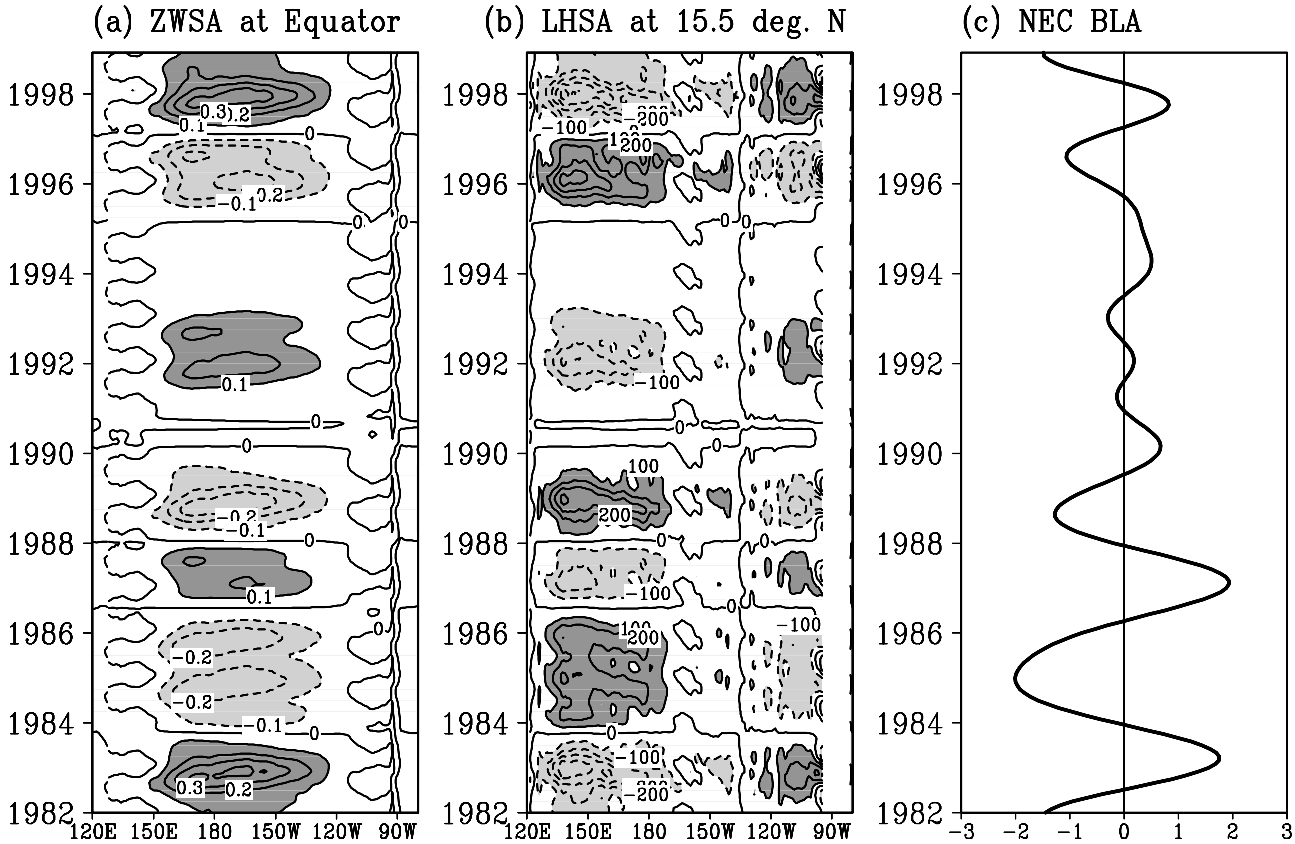

Figure 14. Longitude-time plots of (a) ZWS anomaly mode along the equator, (b) regressed LHS anomaly mode along 15.5°N, and (c) time series of the band-pass filtered (2–7 years), normalized, and depth-averaged NEC bifurcation latitude.

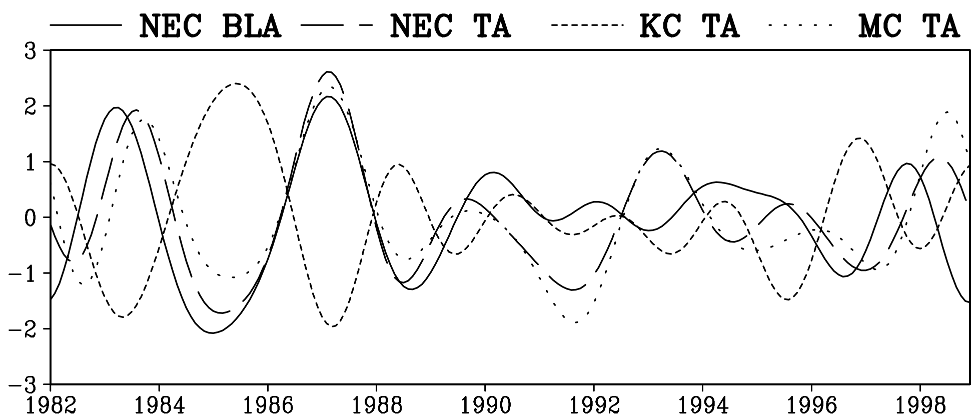

Figure 15. Band-pass filtered (2–7 years), normalized, and depth-averaged NEC bifurcation latitude (NEC BLA) (solid line), band-pass filtered (2–7 years), normalized NEC transport anomaly (NEC TA) (long-dashed line), band-pass filtered (2–7 years), normalized Kuroshio transport anomaly (KC TA) (short-dashed line), and band-pass filtered (2–7 years), normalized MC transport anomaly (MC TA) (dot-dashed line). Here the NEC transport is in a section from 10°N to 18°N along 130°E. The MC transport is from the coast to 130°E along 10°N and the Kuroshio transport is from the coast to 130°E along 18°N.

Table 3. Correlation (Lag in Month) Among NEC BLA, NEC TA, KC TA, and MC TA[a]

	NEC BLA	NEC TA	KC TA	MC TA
NEC BLA	-	*0.73* (−2)	**−0.83** (−1)	*0.54* (−4)
NEC TA	*0.73* (−2)	-	*−0.77* (1)	**0.93** (−1)
KC TA	**−0.83** (−1)	*−0.77* (1)	-	*−0.54* (−3)
MC TA	*0.54* (−4)	**0.93** (−1)	*−0.54* (−3)	-

[a]For NEC BLA, NEC TA, KC TA, and MC TA, refer to the caption of Figure 15. The boldface and italic values indicate that the correlation is 99% and 95% significant, respectively.

penetrate into the midlatitude circulation through the Kuroshio, the western boundary current of the subtropical gyre.

5. Summary and Discussion

[34] Using data from a high-resolution OGCM, we investigated the seasonal and interannual variations of the NEC bifurcation latitude in the Philippine Sea. The model data show a good agreement with existing hydrographic observations and drifter measurements and have a reasonable representation of low-latitude western boundary currents.

[35] In the model, the depth-averaged NEC bifurcates at 15.5°N on the annual average and is well defined in the

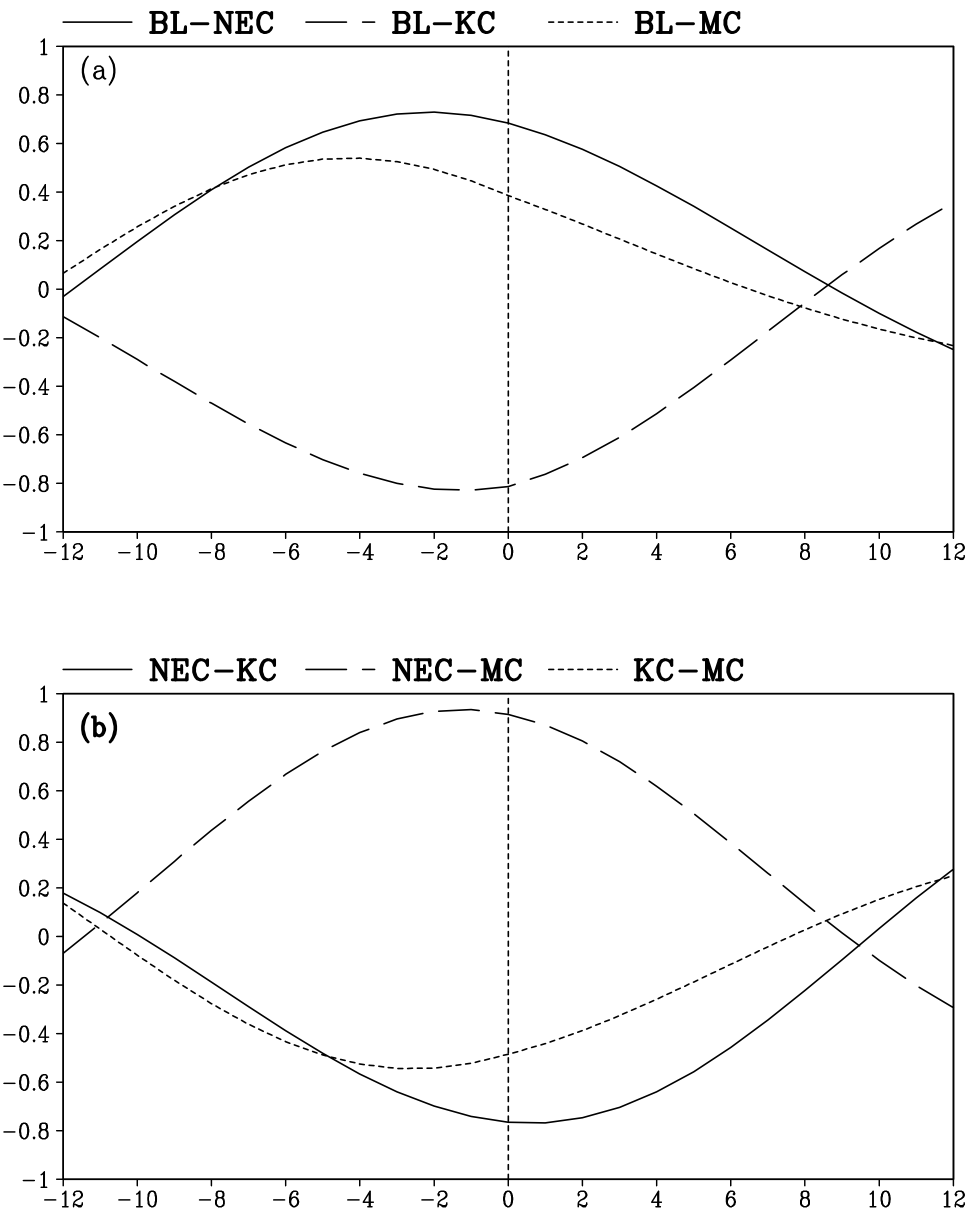

Figure 16. (a) Cross correlations between NEC BLA and NEC TA (BL-NEC) (solid line), between NEC BLA and KC TA (BL-KC) (long-dashed line), and between NEC BLA and MC TA (BL-MC) (short-dashed line). (b) Cross correlations between NEC TA and KC TA (NEC-KC) (solid line), between NEC TA and MC TA (NEC-MC) (long-dashed line), and between KC TA and MC TA (KC-MC) (short-dashed line).

upper 500 m. With depth it varies from about 14.3°N near the surface to about 16.6°N at around 500 m. During the summer the bifurcation moves equatorward with a weak poleward shift with depth, while poleward movement is found in the winter. The seasonal variations of the upper layer LHS are mainly due to local Ekman pumping and westward propagation of the remotely forced Rossby waves. The negative (positive) LHS anomalies caused by the cyclonic (anticyclonic) wind stress curl in the Philippine Sea make the northern branch of the cyclonic gyre circulation shift to the north (south), and move the NEC bifurcation latitude northward (southward). Furthermore, we find that the Ekman drift associated with the northeast monsoon pushes the NEC bifurcation southward more than 1° at the surface, while its northward movement forced by the southwest monsoon is relatively small.

[36] Vertical mode decomposition indicates that the NEC bifurcation variation is governed mostly by the first two vertical modes. For the first mode, the formation of an anomalous circulation gyre is associated with the Ekman pumping and westward propagating Rossby waves, and it causes the NEC bifurcation to move meridionally. The second mode shows that an anomalous circulation gyre at around 150°E is propagating westward relatively slowly, but it weakens rapidly when reaching the southern part of the Philippine coast. The anomalous cyclonic gyre at the coast moves northward from February to June, which can make the NEC bifurcation migrate northward. However, at the same time the larger anticyclonic gyre with positive DHA in the first mode promotes a southward shift in the NEC bifurcation latitude. In contrast, during the winter, a cyclonic gyre at the northern part of the Philippine Sea enhances the northward movement of the NEC bifurcation due to the larger anomalous cyclonic gyre of the first vertical mode. It is also worthwhile to mention that the seasonal vertical slope change in the NEC bifurcation latitude can be understood by the mutual interplay between the first two vertical baroclinic modes.

[37] On the interannual timescale, the meridional migration of the NEC bifurcation latitude is well correlated to the ENSO. Their maximum correlation occurs in the thermocline and exceeds 0.8 in magnitude. The bifurcation occurs at its northernmost position during El Niño years and at its southernmost position during La Niña years. This variation is related to upwelling (downwelling) Rossby waves generated by wind-forcings around the date line of the central tropical Pacific.

[38] The interannual variability of the LHS in the tropical Pacific has been extracted in association with the one dominant mode of the sea surface ZWS through CSEOF and multimodal regression analyses. The first mode of the ZWS anomaly fields shows the temporal evolution of strong westerlies in the equatorial central Pacific, the typical ZWS anomaly patterns of ENSO. The ENSO-related interannual fluctuations are captured in its temporal evolution. The negative (positive) LHS anomalies in the western North Pacific, which influence the NEC bifurcation, are well accounted for by the Philippine Sea anticyclone (cyclone) having the same phase with the ENSO warming (cooling) in the equatorial Pacific. This supports that the NEC bifurcation latitude varies in almost the same phase with ENSO (Figure 11). The northernmost (southernmost) position in the NEC bifurcation latitude corresponds to the westerly (easterly) ZWS anomalies in the central Pacific and the negative (positive) LHS anomalies generated by the anomalous Philippine Sea anticyclone (cyclone).

[39] The interannual fluctuations of the NEC, the MC, and the Kuroshio transports correspond very well with the variation of the NEC bifurcation latitude. All extrema in transports follow the mature phase of the warm and cold episodes of ENSO. Large transports and northward shifts in bifurcation latitude are found in El Niño years. Minimum transports and southward shifts in bifurcation latitude follow the cold phase of ENSO (La Niña). Variations in transport of the NEC and the Kuroshio are well correlated with the variation in the NEC bifurcation latitude, in general, implying that as the bifurcation shifts northward, the NEC and the Kuroshio become stronger, while the MC transport is relatively less affected. Correlation analysis also shows the model transport variations are consistent with those found by previous observations and model studies.

Appendix A: Cyclostationary Empirical Orthogonal Function (CSEOF) Analysis

[40] Space-time data can be written in the form

$$T(\hat{r}, t) = \sum_n T_n(t) \cdot B_n(\hat{r}, t_p),$$

where $B_n(\hat{r},t_p)$ are cyclostationary loading vectors (CSLVs), and $T_n\ (t)$ are their corresponding principal component (PC) time series. The time dependence of CSLVs constitutes an essential difference of the CSEOF analysis from the regular EOF analysis. The name cyclostationary comes from the assumption that CSLVs are periodic in time

$$B_n(\hat{r}, t_p) = B_n(\hat{r}, t_p + d),$$

where d is the nested period with the inherent time, t_p.

[41] The CSLVs are time dependent within time t_p because they are eigenfunctions of periodic and time-dependent covariance statistics. An important point when performing the CSEOF analysis is how to decide the nested period, i.e., the inherent period of covariance statistics. On the basis of the prominent annual cycle, in this study, the nested period is assumed to be 12 months. CSLVs thus represent temporal evolution of spatial patterns during the nested period. The PC time series describe undulation of the CSLVs at timescales larger than the nested period.

Appendix B: Multimodal Regression Analysis

[42] The matching spatial patterns of two physical variables are obtained via a multimodal regression analysis in CSEOF space. Namely, one can solve a regression problem between a target time series, $T_n\ (t)$, and predictor time series, $P_n\ (t)$:

$$T_n(t) = \sum_m \alpha_m P_m(t) + \varepsilon(t).$$

For instance, $T_n\ (t)$ denotes the PC time series of the ZWS anomaly and $P_n\ (t)$ are those of the LHS anomaly. A set of regression coefficients, α_m, are determined such that the variance of regression error, $\varepsilon(t)$, is minimized. In this study, only 10 CSLVs of the ZWS anomaly have been retained for the analysis because they account for more than 90% of total variability and each of the truncated modes explains less than 3% of total variability. The inclusion of more modes does not affect the overall pattern and magnitude. Once the regression coefficients are determined, the spatial pattern of the LHS anomaly evolving together with the ZWS anomaly is given by

$$P_{\mathrm{reg}}\left(\hat{\mathrm{r}}, t_p\right) = \sum_m \alpha_m B_m\left(\hat{r}, t_p\right),$$

where B_m ($\hat{r}$, t_p) are the CSLVs of the predictor variable. More detailed discussion of the regression analysis is given by *Kim and Kim* [2002].

[43] **Acknowledgments.** We thank J. P. McCreary for his helpful discussions. This study was supported by the National Science Foundation through grant OCE00-95906 and by the Frontier Research System for Global Change through their sponsorship of the international Pacific Research Center (IPRC). The drifter data set used in Figure 2 was provided by P. Niiler and N. Maximenko. School of Ocean and Earth Science and Technology (SOEST) contribution 6336, and IPRC contribution IPRC-259.

References

Boulanger, J. P., and C. Menkes (1999), Propagation and reflection in the Pacific Ocean from TOPEX/Poseidon data during the 1992–1998 period, *Clim. Dyn.*, *15*, 205–225.

Donohue, K. A., E. Firing, G. D. Rowe, A. Ishida, and H. Mitsudera (2002), Equatorial Pacific subsurface countercurrents: A model-data comparison in stream coordinates, *J. Phys. Oceanogr.*, *32*, 1252–1264.

Fine, R. A., R. Lukas, F. M. Bingham, M. J. Warner, and R. H. Gammon (1994), The western equatorial Pacific is a water mass crossroads, *J. Geophys. Res.*, *99*, 25,063–25,080.

Fu, L. L., and R. D. Smith (1996), Global ocean circulation from satellite altimetry and high-resolution computer simulation, *Bull. Am. Meteorol. Soc.*, *77*, 2625–2636.

Gill, A. E. (1982), *Atmosphere-Ocean Dynamics*, pp. 342–346, Academic, San Diego, Calif.

Gilson, J., and D. Roemmich (2002), Mean and temporal variability in Kuroshio eostrophic transport south of Taiwan (1993–2001), *J. Oceanogr.*, *58*, 183–195.

Hellerman, S., and M. Rosenstein (1983), Normal monthly wind stress over the world ocean with error estimates, *J. Phys. Oceanogr.*, *13*, 1093–1104.

Hu, D. X., M. C. Cui, T. Qu, and Y. X. Li (1991), A subsurface northward current off Mindanao identified by dynamic calculation, in *Oceanography of Asian Marginal Seas*, *Oceanogr. Ser.*, vol. 54, edited by K. Takano, pp. 359–365, Elsevier, New York.

Ishida, A., Y. Kashino, H. Mitsudera, N. Yoshioka, and T. Kadokura (1998), Preliminary results of a global high-resolution GCM experiment, *J. Fac. Sci. Hokkaido Univ., Ser. VII*, *11*, 441–460.

Kim, K.-Y., and Y. Y. Kim (2002), Mechanism of Kelvin and Rossby waves during ENSO events, *Meteorol. Atmos. Phys.*, *81*, 169–189.

Kim, K.-Y., and G. R. North (1997), EOFs of harmonizable cyclostationary processes, *J. Atmos. Sci.*, *54*, 2416–2427.

Levitus, S. (1982), Climatological atlas of the world ocean, *NOAA Prof. Pap. 13*, 173 pp., U.S. Govt. Print. Off., Washington, D. C.

Lukas, R., E. Firing, P. Hacker, P. L. Richardson, C. A. Collins, R. Fine, and R. Gammon (1991), Observations of the Mindanao Current during the Western Equatorial Ocean Circulation Study, *J. Geophys. Res.*, *96*, 7089–7104.

McPhaden, M. J., et al. (1998), The Tropical Ocean-Global Atmosphere observing system: A decade of progress, *J. Geophys. Res.*, *103*, 14,169–14,240.

Pacanowski, R. (1995), MOM 2 documentation user's guide and reference manual, ver. 1.0, *GFDL Ocean Group Tech. Rep. 3*, Geophys. Fluid Dyn. Lab., Princeton, N. J.

Qiu, B., and T. M. Joyce (1992), Interannual variability in the mid- and low-latitude western North Pacific, *J. Phys. Oceanogr.*, *22*, 1062–1079.

Qiu, B., and R. Lukas (1996), Seasonal and interannual variability of the North Equatorial Current, the Mindanao Current, and the Kuroshio along the Pacific western boundary, *J. Geophys. Res.*, *101*, 12,315–12,330.

Qu, T., and R. Lukas (2003), The bifurcation of the North Equatorial Current in the Pacific, *J. Phys. Oceanogr.*, *33*, 5–18.

Qu, T., H. Mitsudera, and T. Yamagata (1998), On the western boundary currents in the Philippine Sea, *J. Geophys. Res.*, *103*, 7537–7548.

Qu, T., H. Mitsudera, and T. Yamagata (1999), A climatology of the circulation and water mass distribution near the Philippine coast, *J. Phys. Oceanogr.*, *29*, 1488–1505.

Reid, J. L., and R. S. Arthur (1975), Interpretation of maps of geopotential anomaly for the deep Pacific Ocean, *J. Mar. Res.*, *33*, 37–52.

Schott, G. (1939), Die aquatorialen strommungen des westlichen Stillen Ozeans, *Ann. Hydrogr. Mar. Meteorol.*, *67*, 247–257.

Toole, J. M., R. C. Millard, Z. Wang, and S. Pu (1990), Observations of the Pacific North Equatorial Current bifurcation at the Philippine coast, *J. Phys. Oceanogr.*, *20*, 307–318.

Wang, B., R. Wu, and R. Lukas (1999), Roles of the western North Pacific wind variation in thermocline adjustment and ENSO phase transition, *J. Meteorol. Soc. Jpn.*, *77*, 1–16.

Wang, B., R. Wu, and X. Fu (2000), Pacific-East Asian teleconnection: How does ENSO affect East Asian climate?, *J. Clim.*, *13*, 1517–1536.

Yamagata, T., Y. Shibao, and S. Umatani (1985), Interannual variability of the Kuroshio Extension and its relation to the Southern Oscillation/El Niño, *J. Oceanogr. Soc. Jpn.*, *41*, 274–281.

A. Ishida, Ocean Observation and Research Department, Japan Marine Science and Technology Center, 2-15 Natsushima-cho, Yokosuka 237-0061, Japan. (ishidaa@jamstec.go.jp)

T. Jensen, Y. Y. Kim, and T. Qu, International Pacific Research Center, SOEST, University of Hawaii at Manoa, 1680 East West Road, POST Building, Honolulu, HI 96822, USA. (tjensen@hawaii.edu; yykim@hawaii.edu; tangdong@hawaii.edu)

H.-W. Kang, Korea Ocean Research and Development Institute, P.O. Box 29, Ansan, 425-600, Korea. (hwkang@soest.hawaii.edu;)

H. Mitsudera, Institute of Low Temperature Science, Hokkaido University, Hishi 8, Kita 19, Sapporo 060-0819, Japan. (humiom@lowtem.hokudai.ac.jp)

T. Miyama, Frontier Research System for Global Change, 3173-25 Showamachi, Kanazawa-ku, Yokohama City, Kanagawa 236-0001, Japan. (tmiyama@jamstec.go.jp)